LETTERS
https://doi.org/10.1038/s41565-018-0258-0
nature nanotechnology

Mechanically controlled quantum interference in graphene break junctions

Sabina Caneva[1], Pascal Gehring[1], Víctor M. García-Suárez[2,3], Amador García-Fuente[2], Davide Stefani[1], Ignacio J. Olavarria-Contreras[1], Jaime Ferrer[2,3]*, Cees Dekker[1] and Herre S. J. van der Zant[1]*

The ability to detect and distinguish quantum interference signatures is important for both fundamental research and for the realization of devices such as electron resonators[1], interferometers[2] and interference-based spin filters[3]. Consistent with the principles of subwavelength optics, the wave nature of electrons can give rise to various types of interference effects[4], such as Fabry–Pérot resonances[5], Fano resonances[6] and the Aharonov–Bohm effect[7]. Quantum interference conductance oscillations[8] have, indeed, been predicted for multiwall carbon nanotube shuttles and telescopes, and arise from atomic-scale displacements between the inner and outer tubes[9,10]. Previous theoretical work on graphene bilayers indicates that these systems may display similar interference features as a function of the relative position of the two sheets[11,12]. Experimental verification is, however, still lacking. Graphene nanoconstrictions represent an ideal model system to study quantum transport phenomena[13–15] due to the electronic coherence[16] and the transverse confinement of the carriers[17]. Here, we demonstrate the fabrication of bowtie-shaped nanoconstrictions with mechanically controlled break junctions made from a single layer of graphene. Their electrical conductance displays pronounced oscillations at room temperature, with amplitudes that modulate over an order of magnitude as a function of subnanometre displacements. Surprisingly, the oscillations exhibit a period larger than the graphene lattice constant. Charge-transport calculations show that the periodicity originates from a combination of the quantum interference and lattice commensuration effects of two graphene layers that slide across each other. Our results provide direct experimental observation of a Fabry–Pérot-like interference of electron waves that are partially reflected and/or transmitted at the edges of the graphene bilayer overlap region.

We use mechanically controlled break junctions (MCBJs)[18] made from single-layer graphene to measure the electrical conductance of the junction during uniaxial deformation. The MCBJ device consists of a lithographically defined graphene bridge supported on a flexible metal substrate. The substrate is bent, which induces stretching of the graphene bridge until it ruptures. The bending direction can be reversed, which causes the graphene edges to approach each other such that electrical contact can be re-established and thereby allow multiple ($>10^3$) measurements to be performed on a single junction.

Figure 1a–d shows the nanofabrication process for the devices: graphene transfer onto a polymer-coated metal substrate (Fig. 1a), patterning and etching of the graphene bowties (constriction width of 400 nm and length of 750 nm) (Fig. 1b), evaporation of Ti/Au leads (Fig. 1c) and removal of the polymer regions that surround the bowtie (Fig. 1d). The sample is mounted in a three-point bending configuration (Fig. 1e) with a central pushing rod beneath the sample and two counter supports on top of the substrate at both ends. Figure 1f shows a scanning electron microscope image of a device before the measurements were performed, with a magnified view of the junction area in which the graphene bowtie is supported by the polymer structure beneath it. Without the support structure, the edges of the broken junction cannot reform a contact on unbending (Supplementary Fig. 1).

A typical experiment consisted of breaking the graphene bridge at room temperature in air by gradually bending the substrate until a sharp decrease in conductance is observed, dropping from an initial conductance of ~1 G_0, down to the noise level of the set-up (~1×10^{-6} G_0). Here G_0 is the quantum unit of conductance defined as $2e^2/h = 77\,\mu S$, where e is the electron charge and h is Planck's constant. Supplementary Fig. 2 gives a detailed discussion of the conductance calibration. We fabricated 12 junctions that displayed a conductance >1 G_0 before bending: these were used for the MCBJ experiments, four of which exhibited clear conductance oscillations. Examples of the first breaking traces for different samples (C, D and E) are shown in Fig. 2a. Our results are in line with conductance values reported in the literature for monolayer graphene flakes exfoliated in situ with a conductive tip, which are close to 1 G_0 immediately prior to rupture[19].

For sample A, after the graphene bridge was broken, the electrode gap was closed by unbending the substrate (that is, electrical contact restored) and could be re-opened by bending the substrate; consecutive breaking–making traces were thus recorded as a function of time and displacement of the electrodes. A striking feature of these traces is the consistent conductance recovery from ~1×10^{-6} G_0 to ~1 G_0 in each cycle, which indicates excellent mechanical stability and reproducibility of the measurement (Fig. 2b,c). Remarkably, large periodic oscillations appeared in the high-conductance range, with drops of almost an order of magnitude between the maxima. These features are similar to the current modulations observed in suspended graphene bilayers during indentation with an atomic force microscopy tip, albeit with much larger amplitudes[20]. These oscillations are not observed for the first breaking trace and only appear during all the following cyclings of the junction. To convert the time axis units into horizontal displacement, we recorded 20 current–voltage (I–V) experiments for fixed displacements in the conductance regime from the noise level up to ~1×10^{-4} G_0 for this sample. Given that the I–V measurements in this range display

[1]Kavli Institute of Nanoscience, Delft University of Technology, Delft, The Netherlands. [2]Departamento de Física, Universidad de Oviedo, Oviedo, Spain. [3]Nanomaterials and Nanotechnology Research Center, CSIC – Universidad de Oviedo, Oviedo, Spain. *e-mail: ferrer@uniovi.es; H.S.J.vanderzant@tudelft.nl

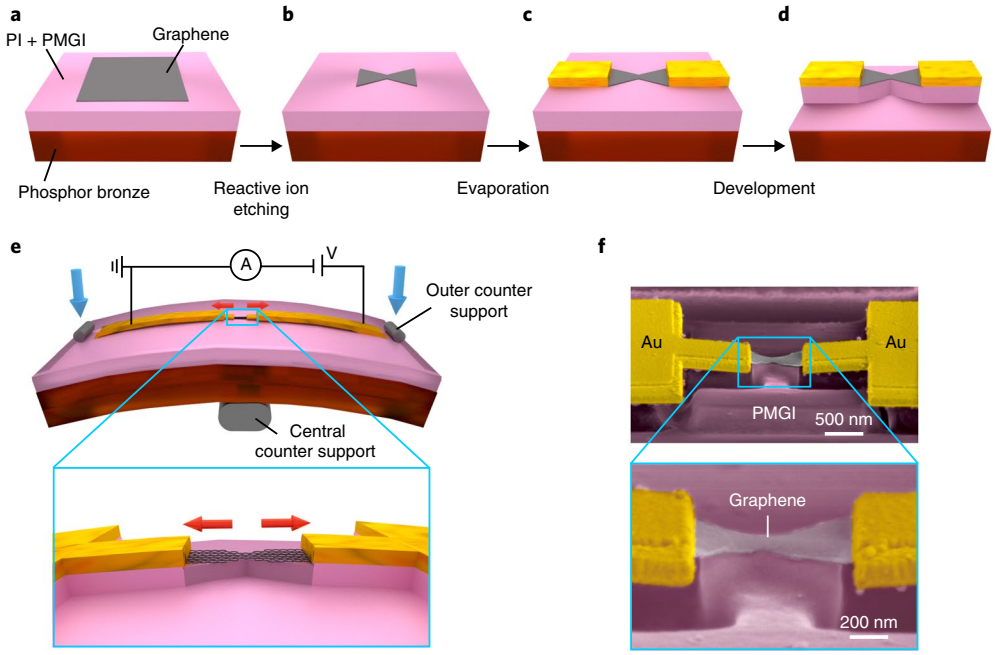

Fig. 1 | Nanofabrication of graphene MCBJs. a, Transfer of monolayer graphene on top of the phosphor bronze substrate coated with polyimide (PI) and polymethylglutarimide (PMGI) insulating layers. **b**, Reactive ion etching of the graphene into a bowtie shape by an O_2 plasma (400 nm constriction width and 750 nm Au electrode separation). **c**, Evaporation of the leads (Ti(5 nm)/Au(70 nm)). **d**, Development of the sample in ethyl lactate to produce a supported graphene bridge. **e**, Schematic representation of the MCBJ measurement set-up. **f**, False-colour scanning electron microscope image of a typical device before the measurements were performed (top) and a magnified view of the junction (bottom).

tunnelling characteristics, the curves were fitted with a Simmons model[21] from which the gap size can be estimated (Supplementary Figs. 3 and 4). Figure 2d shows the alignment of 1,000 consecutive breaking measurements as a function of displacement for sample A. The close similarity of all the traces is evident from the vertical lines along the displacement axis, which shows that these oscillations are not merely random noise, but exhibit a defined periodicity. A two-dimensional (2D) histogram was constructed from the aligned breaking traces (Fig. 2e), which clearly shows the same modulations present in the individual curves. The corresponding alignment and 2D histogram for the making traces are shown in Supplementary Fig. 5.

Figure 3a shows representative breaking traces for two different samples that display oscillations. For each sample, 1,000 traces were summed and the derivative with respect to the distance was calculated to determine the periodicity of the signal. Figure 3b shows the linear fit for the peak number as a function of peak position (peaks are identified by the maxima and the minima in the derivative), from which we estimate a typical oscillation periodicity of 0.68 nm for sample A (blue curve) and 0.89 nm for sample B (magenta curve).

Figure 3c displays the average of ten breaking traces at room temperature in air and vacuum (10^{-6} mbar) for sample F. We observed that the period increased from 0.60 nm to 0.68 nm going from air to vacuum (Fig. 3d). To relate this change to a shift in the Fermi wavevector, k_F, and therefore doping level, we fabricated similar graphene bowtie structures on SiO_2(285 nm)/Si and measured the source–drain current as a function of gate voltage for analogous conditions. For the sample in the inset of Fig. 3d, when exposed initially to air, the Dirac point (V_{Dirac}) was at ~70 V. In vacuum, V_{Dirac} shifts to ~50 V. We ascribe the higher V_{Dirac} in air to the well-known p-type doping due to the adsorption of oxygen and water molecules during ambient exposure[6]. From the Fabry–Pérot interference condition $dk_F = \pi$, we can compare the experimentally derived periodicity ratio $d_{vac}/d_{air} = 1.33$ with the ratio $\sqrt{V_{Dirac,air}/V_{Dirac,vac}} = 1.84 \pm 0.61$ as determined from measuring seven gated samples (Supplementary Table 1). Hence, the periodicity falls within this range. The $\sqrt{V_{Dirac,air}/V_{Dirac,vac}}$ values are extracted given $k_F = \sqrt{n}$, and $n = C_{ox}(V_{gate} - V_{Dirac})/e$, where n is the carrier concentration, C_{ox} is the back-gate capacitance and V_{gate} is set to zero (no gate voltage is applied in the MCBJ experiments). Our findings can be understood from the fact that the less doped graphene in vacuum has a wavevector that is smaller than the wavevector for the air-exposed sample. Using the Fabry–Pérot interference condition, this would result in larger oscillation periodicities for the vacuum-exposed sample, which is in line with our experiments. We can thus exclude the lattice periodicity effect as the only origin of the conductance oscillations. The inset in Fig. 3d shows a schematic of the low-energy dispersion relation for p-type doped graphene and the relative change in the wavevector with doping level.

To unveil the physical origin of the observed conductance oscillations, we performed density functional theory (DFT) simulations of two graphene sheets sliding rigidly against each other and calculated the conductance for each relative displacement. Figure 4a shows simulated breaking/making cycles in which two sheets are moved relative to each other in the zigzag direction. Given that the experiments were performed in ambient conditions, the sheets were terminated at the contact region by armchair edges that were either passivated by hydrogen atoms (blue curve) or carboxyl groups (magenta curve). The shape of these conductance traces agrees remarkably well with the experiments; the traces start at ~1×10^{-6} G_0, saturate at around 0.5 G_0 and show conductance oscillations of very similar shape and period. These quantum interference oscillations should appear if the Fabry–Pérot interference condition $k_F d_{QI} = \pi$ is fulfilled[20], where $k_F = 2\pi/3c$ is the Fermi wavevector along the zigzag direction, d_{QI} is the Fabry–Pérot period and $c = 0.246$ nm is the graphene lattice constant. The oscillation period in the zigzag direction should therefore be $d_{QI} = 3/2c = 0.37$ nm. These oscillations cannot be seen directly in Fig. 4a because they overlap with those that originate from the lattice periodicity effect, which has a

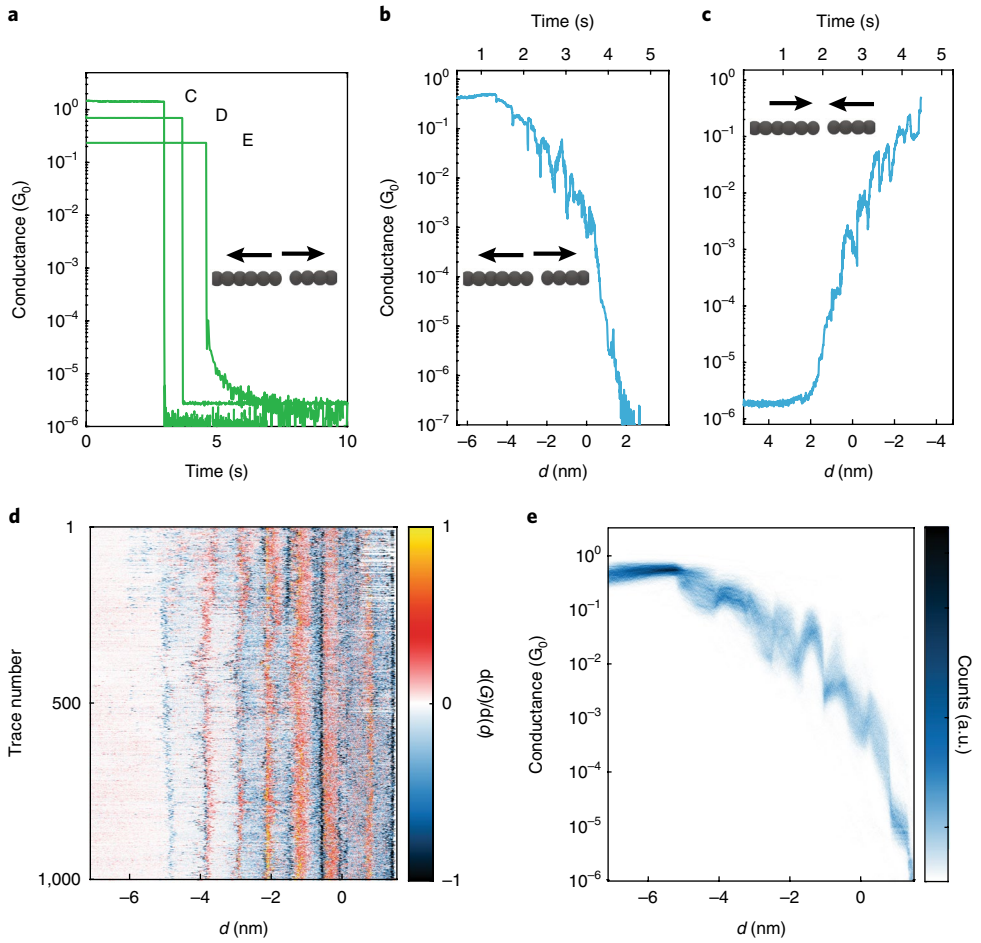

Fig. 2 | Electromechanical measurements reveal conductance oscillations. a, Conductance, plotted on a logarithmic scale, as a function of time for the first breaking trace in samples C, D and E measured at a bias voltage of 0.1 V. **b**,**c**, Example of typical breaking (**b**) and making (**c**) traces as a function of displacement and time during the cycling of sample A, which shows periodic oscillations in the high-conductance range (10^{0}–10^{-4} G_0). The arrows indicate the direction of the measurements. We define the zero displacement ($d = 0$) as the position in which the last C atom of the left graphene edge is located directly beneath the last C atom of the right graphene edge. From DFT calculations, such a configuration yields a conductance between 10^{-2} and 10^{-4} G_0. The schematics in panels **a**,**b**,**c** represent a side view of the two graphene edges with the arrows indicating the displacement direction. **d**, Alignment of 1,000 traces from sample A using a cross-correlation method in which each trace is shifted such that the overlap with all the other traces is maximised. **e**, A 2D histogram of the conductance as a function of displacement constructed from 1,000 consecutive traces from sample A measured at room temperature in air. No trace selection was performed. For all the data presented in the main text, the contact resistance is subtracted from the measured conductances (Supplementary Fig. 2). a.u., arbitrary units.

period equal to c in the zigzag direction (Supplementary Fig. 11 and Supplementary Table 2).

Figure 4b allows the two types of oscillations to be disentangled by plotting the magnitude of the oscillation amplitude, measured as the ratio between the maximum and minimum values of the conductance of each oscillation (G_{max}/G_{min}) in Fig. 4a, as a function of the distance between two corresponding minima. We found that our data points cluster into three groups. The first group has a conductance ratio of ~1–2 and an oscillation period equal to c, which is much smaller than the periods measured in our experiments. These oscillations originate from the lattice periodicity effect. The amplitudes of the second group of oscillations are larger, with a conductance ratio of ~10. This group clusters around $d_{QI} = 0.37$ nm and corresponds to Fabry–Pérot interferences. The third group clusters at a period of $0.74\,\text{nm} = 3c \approx 2d_{QI}$. Here the two shorter oscillations combine, which results in a beating pattern with a larger oscillation period and very big amplitudes with conductance ratios of ~100. Supplementary Information describes the conductance traces for bilayers that slide along the armchair and chiral (4,1) directions (Supplementary Figs. 6–10). The overall picture that emerges is coherent: the length scale of the oscillations due to the lattice periodicity effect is of the order of c or a fraction of it, for example, much smaller than the period measured in our experiments. In contrast, Fabry–Pérot oscillations, as well as the combined effect of the Fabry–Pérot and potential oscillations, have longer periods of at least 0.4 nm and even reach 1 nm, which is consistent with our experimental findings.

Figure 4c shows a contour plot of the electron transmission through junction T as a function of the energy of the impinging electrons E and the displacement d. The plot shows both oscillations and interference patterns. A first set of oscillations becomes periodic and independent of energy for a sufficiently negative d (that is, for an increased bilayer overlap region), with a period equal to the lattice spacing in the zigzag direction. These oscillations originate from the periodic nature of the hopping integrals that bridge the two sheets, which modify the sheet band structure. We found a second set of oscillation lines that runs diagonally and bends towards the bottom left in the plot (that is, a large bilayer overlap and negative energy). These are caused by the destructive interference of waves partially confined in the bilayer region.

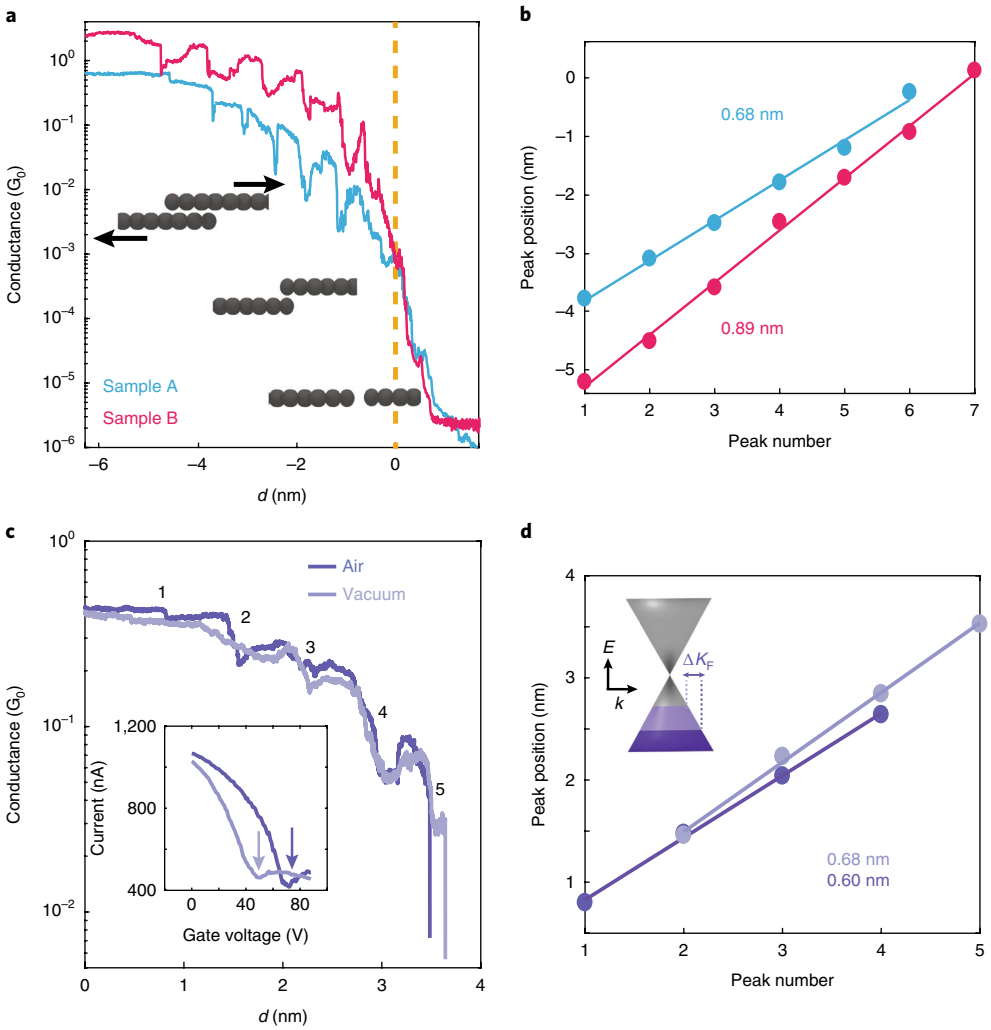

Fig. 3 | Analysis of the oscillation periodicities. a, Typical breaking trace for samples A and B that display oscillations. The vertical dotted line indicates the displacement, *d*, at which the graphene contact is broken, defined as $d=0$. The three schematics below the blue curve represent a side view of the two graphene edges, showing the bilayer overlap region, sliding of the layers and opening of the nanogap. **b**, Peak position plotted as a function of peak number for the first 6 and 7 peaks in samples A and B, respectively. The experimental data points are shown as blue and magenta circles. The line of best fit provides an estimate of the oscillation periodicity: 0.68 nm for sample A and 0.89 nm for sample B. **c**, Comparison of the oscillations in the 10^{-1} G_0 to 10^{-3} G_0 conductance regime for sample F exposed to air and vacuum (10^{-6} mbar) at room temperature. We recorded 100 breaking traces for each experiment. Given the measured conductance range, we cannot define the same $d=0$ reference as in **a** and **b**. We have thus arbitrarily set the zero at the start of the traces. Inset: the source–drain current as a function of gate voltage shows Dirac curves for a graphene bowtie on SiO_2/Si exposed to air and vacuum (10^{-5} mbar vacuum with a mild annealing step (Methods)). **d**, The peak position as a function of peak number (labelled 1–5 in **c**) shows a larger period for the vacuum-exposed sample. Inset: schematic of the energy–momentum relation, *E*–*k*, which depicts the change in k_F with doping level.

Figure 4d shows the calculated transmission contour plot as a function of E and d based on the 1D tight-binding model in Fig. 4e, in which both vertical and curved oscillations are clearly discernible, resulting from changes in the lattice commensuration and antiresonances respectively. We model the bilayer system as two oppositely oriented semi-infinite chains that slide on top of each other. An algebraic analysis of the model shows that electron waves are partly reflected and/or transmitted at the edges of the chain overlap region of length $D=(N+1)c\approx d$, where N and c are the number of atoms in this overlap region and the lattice constant, respectively. This results in destructive interference whenever $k_F(N+1)c=n\pi$, where n is a positive integer. The periodic vertical oscillations in the contour vanish when we set the interchain hopping integrals t_{ij} to be constant (that is, remove the shifts in the lattice commensuration); however, the curved interference pattern remains. Supplementary Information describes additional 1D models and further algebraic details that support this analysis (Supplementary Figs. 13 and 14). These results are in good agreement with previous theoretical studies on the conductance variation in bilayer graphene as a function of overlap length[22].

In conclusion, we presented graphene MCBJs and demonstrated that the junction conductance can be reversibly switched by almost six orders of magnitude during 1,000 opening–closing cycles, which attests to the high mechanical stability of the MCBJ device. Although electronic switching has been demonstrated for electroburned graphene nanoribbons, the switching behaviour was attributed to the formation and/or rupture of carbon chains[23,24]. We additionally observed large conductance oscillations as a function of nanometre displacement between two overlapping graphene sheets during cycling. This is in contrast to the featureless conductance traces in twisted graphene tunnelling junctions reported in the literature[25]. Our findings, supported by DFT and tight-binding calculations, are a direct experimental observation of the quantum interference of standing waves in sliding bilayer graphene at room temperature.

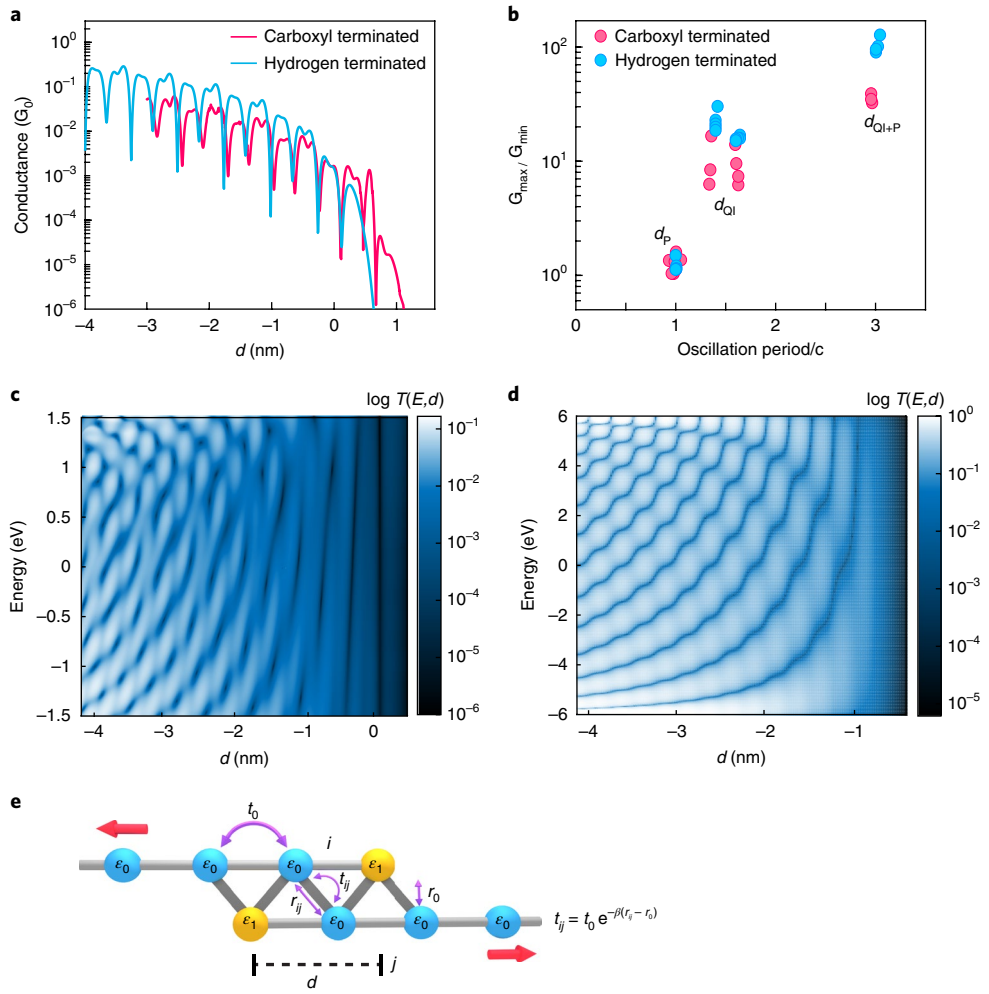

Fig. 4 | DFT and tight-binding calculations of sliding graphene bilayers. a, Examples of two calculated breaking traces for graphene sheets that slide along the zigzag direction and are terminated with armchair edges. The conductance is plotted on a logarithmic scale as a function of the displacement *d*. The edges were passivated by hydrogen and carboxyl groups and the intersheet distance was ~0.45 nm. **b**, Plot of the ratio of the maximum and minimum values of the conductance of the oscillations, G_{max}/G_{min}, as a function of the distance between adjacent minima normalized by the lattice constant *c* for each of the oscillations in **a**. d_P, d_{QI} and d_{QI+P} denote the periodicity due to the lattice periodicity effect, quantum interference effects and the combination of the two effects, respectively. The oscillation with the largest amplitude has a period $d_{QI+P} \approx 0.74$ nm. **c**, Contour plots of the decimal logarithm of the transmission function $\log_{10}(T(E,d))$ as a function of the displacement *d* and of the energy *E* referenced to the Fermi energy E_F for the hydrogen-terminated bilayer in **a**. **d**, Contour plots of $\log_{10}(T(E,d))$ of the model in **c** as a function of *d* and *E* in which the parameters were adjusted to fit the experimental distances, graphene hopping integrals and tunnelling decay lengths. The plot displays the different types of conductance oscillations: a vertical periodic pattern due to shifts in lattice commensuration (white areas) and destructive quantum interferences (dark blue features). These are also apparent in **c**. **e**, Schematic of the tight-binding model showing the relevant interchain (r_0) and interatomic (r_{ij}) distances, the chain (ε_0) and edge on-site (ε_1) energies and the intrachain (t_0) and interchain (t_{ij}) hopping parameters. $D=(N+1)c \approx d$ is the overlap length, and *N* and *c* are the number of atoms in this overlap region and the lattice constant, respectively.

Our MCBJ platform allows the intriguing possibility to tune the junction conductance over a large range with a purely mechanical tuning knob, and thus has a potential use as a nanoelectromechanical system[20,26]. Furthermore, given that the gap size can be adjusted with exceptionally high precision and stability, we envisage that graphene MCBJs could be used as a powerful tool for quantum tunnelling-based sensing of (bio)molecules[27,28].

Online content

Any methods, additional references, Nature Research reporting summaries, source data, statements of data availability and associated accession codes are available at https://doi.org/10.1038/s41565-018-0258-0.

Received: 14 March 2018; Accepted: 9 August 2018;
Published online: 17 September 2018

References

1. Liang, W. et al. Fabry–Pérot interference in a nanotube electron waveguide. *Nature* **411**, 665–669 (2010).
2. Ji, Y. et al. An electronic Mach–Zehnder interferometer. *Nature* **422**, 415–418 (2003).
3. Lundeberg, M. B. & Folk, J. A. Spin-resolved quantum interference in graphene. *Nat. Phys.* **5**, 894–897 (2009).
4. Darancet, P., Olevano, V. & Mayou, D. Coherent electronic transport through graphene constrictions: subwavelength regime and optical analogy. *Phys. Rev. Lett.* **102**, 2–5 (2009).
5. Shytov, A. V., Rudner, M. S. & Levitov, L. S. Klein backscattering and Fabry–Pérot interference in graphene heterojunctions. *Phys. Rev. Lett.* **101**, 156804 (2008).
6. Gehring, P. et al. Quantum interference in graphene nanoconstrictions. *Nano Lett.* **16**, 4210–4216 (2016).
7. Russo, S. et al. Observation of Aharonov–Bohm conductance oscillations in a graphene ring. *Phys. Rev. B* **77**, 1–5 (2008).
8. Grace, I. M., Bailey, S. W. & Lambert, C. J. Electron transport in carbon nanotube shuttles and telescopes. *Phys. Rev. B* **70**, 153405 (2004).

9. Jiang, H. et al. Carbon nanotube electronic displacement encoder with sub-nanometer resolution. *J. Comput. Theor. Nanosci.* **4**, 574–577 (2007).
10. Tunney, M. A. & Cooper, N. R. Effects of disorder and momentum relaxation on the intertube transport of incommensurate carbon nanotube ropes and multiwall nanotubes. *Phys. Rev. B* **74**, 075406 (2006).
11. Popov, A. M. et al. AA stacking, tribological and electronic properties of double-layer graphene with krypton spacer. *J. Chem. Phys.* **139**, 154705 (2013).
12. Poklonski, N. A. et al. Graphene-based nanodynamometer. *J. Comput. Theor. Nanosci.* **10**, 141–146 (2013).
13. Miao, F. et al. Phase-coherent transport in graphene quantum billiards. *Science* **317**, 1530–1533 (2007).
14. Zhang, Y., Tan, Y., Stormer, H. L. & Kim, P. Experimental observation of the quantum Hall effect and Berry's phase in graphene. *Nature* **438**, 201–204 (2005).
15. Sadeghi, H. et al. Conductance enlargement in picoscale electroburnt graphene nanojunctions. *Proc. Natl Acad. Sci. USA* **112**, 2658–2663 (2015).
16. Berger, C. et al. Electronic confinement and coherence in patterned epitaxial graphene. *Science* **312**, 1191–1197 (2006).
17. Young, A. F. & Kim, P. Quantum interference and Klein tunnelling in graphene heterojunctions. *Nat. Phys.* **5**, 222–226 (2009).
18. Frisenda, R., Janssen, V. A. E. C., Grozema, F. C., van der Zant, H. S. J. & Renaud, N. Mechanically controlled quantum interference in individual π-stacked dimers. *Nat. Chem.* **8**, 1099–1104 (2016).
19. Kinikar, A. et al. Quantized edge modes in atomic-scale contacts in graphene. *Nat. Nanotech.* **12**, 564–568 (2017).
20. Benameur, M. M. et al. Electromechanical oscillations in bilayer graphene. *Nat. Commun.* **6**, 8582 (2015).
21. Simmons, J. G. Generalized formula for the electric tunnel effect between similar electrodes separated by a thin insulating film. *J. Appl. Phys.* **34**, 1793 (1963).
22. González, J. W., Santos, H., Pacheco, M., Chico, L. & Brey, L. Electronic transport through bilayer graphene flakes. *Phys. Rev. B* **81**, 195406 (2010).
23. Zhang, H. et al. Visualizing electrical breakdown and on/off states in electrically switchable suspended graphene break junctions. *Nano Lett.* **12**, 1772–1775 (2012).
24. Sarwat, S. G. et al. Scaling limits of graphene nanoelectrodes. *Nano Lett.* **17**, 3688–3693 (2017).
25. Bellunato, A. et al. Dynamic tunneling junctions at the atomic intersection of two twisted graphene edges. *Nano Lett.* **18**, 2505–2510 (2018).
26. Isacsson, A. Nanomechanical displacement detection using coherent transport in graphene nanoribbon resonators. *Phys. Rev. B* **84**, 125452 (2011).
27. Heerema, S. J. & Dekker, C. Graphene nanodevices for DNA sequencing. *Nat. Nanotech.* **11**, 127–136 (2016).
28. Di Ventra, M. & Taniguchi, M. Decoding DNA, RNA and peptides with quantum tunnelling. *Nat. Nanotech.* **11**, 117–126 (2016).

Acknowledgements

S.C. acknowledges a Marie Skłodowska-Curie Individual Fellowship under grant BioGraphING (ID 798851) and P.G. acknowledges a Marie Skłodowska-Curie Individual Fellowship under grant TherSpinMol (ID 748642) from the European Union's Horizon 2020 research and innovation programme. This work was supported by the Graphene Flagship (a European Union's Horizon 2020 research and innovation programme under grant agreement no. 649953), the Marie Curie ITN MOLESCO and an ERC advanced grant (Mols@Mols No. 240299). The research by V.M.G.-S., A.G-F. and J.F. was funded by the project FIS2015-63918-R from the Spanish government.

Author contributions

S.C., H.S.J.Z. and C.D. conceived the idea and designed the experiments. S.C. developed the nanofabrication protocol. S.C., I.J.O.-C., D.S. and P.G. performed the break junction experiments. P.G. and S.C. performed the graphene gating measurements. P.G. designed and implemented the cross-correlation method and performed the *I*–*V* data analysis. J.F. supervised the theoretical research work. V.M.G.-S. and J.F. conceived the simulations. A.G.-F. and V.M.G.-S. carried out the DFT calculations. V.M.G.-S. and J.F. carried out the tight-binding calculations. J.F. developed the algebraic analysis of the charge transport model and of the interference conditions. All the authors participated in discussions and co-wrote the paper.

Competing interests

The authors declare no competing interests.

Additional information

Supplementary information is available for this paper at https://doi.org/10.1038/s41565-018-0258-0.

Reprints and permissions information is available at www.nature.com/reprints.

Correspondence and requests for materials should be addressed to J.F. or H.S.J.Z.

Publisher's note: Springer Nature remains neutral with regard to jurisdictional claims in published maps and institutional affiliations.

Methods

Nanofabrication of graphene MCBJs. The MCBJ devices were prepared using the following protocol, based on a previously published protocol[29]. Flexible phosphor bronze chips ($1 \times 2\,cm^2$) were cleaned by sonicating for 5 min in acetone and subsequently in isopropanol. An adhesion promoter (VM651) was spin coated on the phosphor bronze at 2,500 revolutions per minute (r.p.m.) and baked for 1 min at 110 °C. An insulating layer of polyimide was spin coated on top at 800 r.p.m. and baked in a vacuum oven at 300 °C for 30 min. A layer of lift-off resist (SF7) was spin coated as the topmost layer at 4,500 r.p.m. and baked for 5 min at 180 °C. A poly(methylmethacrylate) (PMMA) resist layer (A6 495k) was spin coated at 4,500 r.p.m. and baked at 180 °C for 2 min. Markers were patterned on the chip by electron-beam lithography (EBPG 5000+ (Raith)). The sample was developed in xylene at room temperature for 30 s and then blow dried in N_2. A 60 nm thick W layer was sputtered and lift-off was performed in xylene at 80 °C for 10 min, followed by blow drying in N_2. PMMA-covered monolayer chemical vapour deposition graphene (purchased from Graphenea on Cu foil) was transferred using the wet etching process in ammonium persulfate. The PMMA was removed by placing the sample in xylene at 80 °C for 10 min. A new layer of PMMA (A6 495k) was spin coated at 4,500 r.p.m. and baked at 180 °C for 2 min. The graphene was patterned into bowtie shapes by exposing the region around it (electron dose of $850\,\mu C\,cm^{-2}$). The sample was developed in xylene at room temperature for 30 s. The exposed graphene regions were etched by reactive ion etching in an O_2 plasma (5 mbar, 20 W, 20 sccm, 30 s). The PMMA was removed by placing the sample in xylene at 80 °C for 10 min. A double-layer resist (PMMA A6 495k and A3 950k) was spin coated at 4,500 r.p.m. and baked at 180 °C for 2 min after each layer. Leads and pads were patterned (electron dose of $850\,\mu C\,cm^{-2}$) and the sample was developed in xylene at room temperature for 30 s. Electron-beam evaporation was used to deposit Ti(5 nm)/Au(70 nm). Lift-off was performed in xylene at 80 °C for 30 min. Finally, the sample was dipped in ethyl lactate for 30 s to produce an undercut and then rinsed twice in deionized water.

MCBJ experiments. Large Au pads that connected the graphene bowties were covered in a silver conducting paste and the chip was mounted in a custom-made break junction set-up. The conductance was recorded as a function of time at a bias voltage of 0.1 V while a brushless servo-motor bent the sample. Once the conductance dropped to the noise level, the motor was stopped. A voltage was then applied on the piezo element to verify whether the junction could be cycled (that is, recover a high-G state by decreasing the piezo voltage and breaking once more by applying a voltage). Once the cycling was confirmed, a conductance histogram measurement that comprised 1,000 consecutive traces was set up. All the experimental plots display the conductance of the graphene junction only (that is, the contact resistance is subtracted by measuring in a four-point probe scheme). Measurements were performed at room temperature in air and in vacuum (10^{-6} mbar).

Measurements with the back gate. For the determination of the effect of doping between air and vacuum measurements, graphene bowtie samples on silicon back-gate substrates (SiO_2(285 nm)/Si) were prepared based on a previously published protocol[6]. The samples were measured in air and in vacuum (10^{-5} mbar) using home-built low-noise d.c. electronics. The gate voltage was swept from −20 V to 90 V, and a bias of 10 mV was applied between the source and drain electrodes. To account for the very high current per unit width, on the order of 0.5–10 A mm^{-1} (using $G = G_0$ and a contact width of about 1–20 nm), that can arise in very narrow constrictions formed in the graphene break junction experiments, a current of 100 μA (which corresponds to a current per unit width of about 0.5 A mm^{-1} in the constriction area) was passed through the junction for several minutes in vacuum.

DFT simulations. Ab initio simulations of graphene MCBJs were carried out with the DFT program SIESTA[30]. Here, two sheets oriented along the zigzag, armchair or chiral directions are terminated with armchair, zigzag or complementary chiral edges. The edges are passivated by hydrogen or carboxyl groups. Closing MCBJ cycles are simulated where the two sheets approach each other in steps of 0.05 Å, starting from a distance at which the tunnelling rate is zero. The conductance and electron transmission calculations were performed with the quantum transport code GOLLUM[31]. Supplementary Information gives further details, as well as sketches of the MCBJ geometries of the simulations (Supplementary Figs. 6 and 13).

The DFT code SIESTA is publicly available at https://launchpad.net/siesta.

Tight-binding modelling. The electrical transport features of the several 1D models were analysed algebraically and/or numerically as discussed in the main text and in Supplementary Information (Supplementary Figs. 12 and Fig. 13).

GOLLUM is a quantum transport package that is freely available upon request at http://www.physics.lancs.ac.uk/gollum/.

Data availability

The data that support the plots within this paper and other findings of this study are available from the corresponding authors upon reasonable request.

References

29. Rickhaus, P. et al. Ballistic interferences in suspended graphene. *Nat. Commun.* **4**, 2342 (2013).
30. Soler, M. J. et al. The SIESTA method for ab initio order-N materials simulation. *J. Phys. Condens. Matter* **14**, 2745 (2002).
31. Ferrer, J. et al. GOLLUM: a next-generation simulation tool for electron, thermal and spin transport. *New J. Phys.* **16**, 093029 (2014).